Density functional simulations of decomposition pathways of Ge-rich GeSbTe alloys for phase change memories

O. Abou El Kheir, D. Dragoni, and M. Bernasconi
Dipartimento di Scienza dei Materiali, Università di Milano-Bicocca, Via R. Cozzi 55, I-20125, Milano, Italy

Germanium rich GeSbTe alloys have recently emerged as promising materials for embedded phase change memories of interest for applications in the automotive sector thanks to the high crystallization temperature of their amorphous phase. Crystallization of Ge-rich GeSbTe alloys can lead to phase separation with segregation of crystalline Ge. The inhomogeneity of the resulting system brings, however, some drawbacks such as the drift of the electrical resistance with time of the crystalline phase. To mitigate these effects, a better understanding of the decomposition process is needed. In this work, we performed density functional calculations on possible decomposition pathways of the $Ge_5Sb_2Te_3$ alloy as an example of Ge-rich GeSbTe alloy on the Ge-Sb_2Te_3 pseudobinary line. The energetics of the transformation into crystalline Ge and a less Ge-rich alloy is investigated as well as the structural, electronic and vibrational properties of some possible decomposition products such as $Ge_3Sb_2Te_3$ or $Ge_2Sb_2Te_1$, among several others, in both the crystalline and amorphous phases.

I. INTRODUCTION

Phase change materials are chalcogenide alloys suitable to switch reversibly between crystalline and amorphous phases on a very short time upon Joule heating[1]. This feature is exploited in the realization of non-volatile electronic memories, named phase change memories (PCM)[2–4], which have been commercialized since 2017 by the companies Intel and Micron. These devices, based on a 3D-Xpoint^{TM} cross-bar technology[5], entered the market as the first realization of the so-called storage class memories designed to fill the performance gap between the fast but volatile dynamic random access memories (DRAM) and the nonvolatile but slow flash storage[6].

The operation of the device is based on the application of current pulses suitable to induce the melting of the crystal and its subsequent amorphization (reset) or the recrystallization of the amorphous phase (set). The logical information of the memory can be encoded thanks to the large difference in the electrical resistivity of the two phases that can be easily read at low bias.

More recently, PCMs are also emerging for applications in embedded nonvolatile memories[7], in particular for the automotive sector. For this latter application, the operation temperature of the device is higher than that of conventional stand-alone PCMs which imposes the use of materials with crystallization temperature T_X higher than that of the flagship $Ge_2Sb_2Te_5$ (GST225) phase change alloy. The mostly used GST225 alloy has indeed a crystallization temperature in the range 420-440 K[8]; this alloy can be seen as a pseudobinary compound along the GeTe-Sb_2Te_3 tie line[1].

Ge-rich GeSbTe (GST) alloys off the pseudobinary GeTe-Sb_2Te_3 tie line have been engineered for application in embedded memories. In fact, it was shown that the crystallization temperature can be increased up to 570 K by raising the Ge content along the Ge-(Sb_2Te_3) pseudobinary line[9]. Ge-rich alloys on the Ge-$Ge_2Sb_2Te_5$[10] or Sb-GeTe[11,12] pseudobinary lines have been also optimized to improve data retention (stability of the amorphous phase) for embedded applications. The higher crystallization temperature of these alloys also guarantees code integrity of the memory during soldering.

The crystallization of as-deposited Ge-rich GST alloys actually leads to the formation of crystalline Ge and a face-centered-cubic crystal[9]. Similar results have been obtained in Ref. 13 where crystalline GST225 and Ge were identified as the result of crystallization of a film of Ge-rich GST alloys. In this latter work, the higher crystallization temperature of Ge-rich GST was ascribed to the phase separation with segregation of crystalline Ge which slows down the process due to mass transport. Whether this is the case also for the set process of the memory is, however, unclear. On the other hand, phase separation with the formation of crystalline Ge and a less Ge-rich alloy is observed also in the initialization (forming) of PCM cells[14,15]. Moreover, it has been noted that the kinetics of the crystallization depends on the preparation conditions, in fact crystallization is different in the as-deposited and melt-quenched amorphous phase and in the melt[16].

The increase in data retention with Ge enrichment has, however, some disadvantages such as a resistance drift in the crystalline phase aside from the most common drift in the amorphous phase due to aging[7,17]. To better control eventual detrimental effects of the phase separation, a better knowledge of the crystallization process and of the resulting crystal compositions and structures is actually needed.

In this work, we present a theoretical study based on density functional theory (DFT) of possible decomposition pathways of the $Ge_5Sb_2Te_3$ (GST523) alloy that it is the first, i.e., the less Ge-rich, of a series of Ge-rich alloys with high T_X on the Ge-Sb_2Te_3 pseudobinary line investigated experimentally in Ref. 9. GST523 was also found among the most abundant products of the crystallization of very Ge-rich alloys (e.g. $Ge_{18}Sb_2Te_5$) used in several demonstrators for embedded PCMs[16]. In this respect, we have to consider that the reactions of relevance for the operation of the memory might not lead to the thermodynamically most stable products, but to the metastable systems due kinetic hindrances. For instance, amorphous $GeSb_2Te_4$ (GST124) and GST225 alloys in PCMs crystallize into the metastable cubic phase and not in their most stable trigonal phases. The cubic crystal is always metastable, also at the temperature of the set process of the memory which is tuned in between the glass transition and the

melting temperatures where crystal growth velocity is maximal. The formation of the metastable cubic phase instead of the thermodynamically stable trigonal ones is due to the short time span on which the crystallization takes place during set. The crystalline nuclei always form in the cubic phase as also shown by atomistic simulations[3]. In fact, it is much easier for the amorphous network to turn into the cubic phase with a random distribution of stoichiometric vacancies in the cation sublattice. The formation of the trigonal phase requires instead the ordering and coalescence of these vacancies to form van der Waals gaps between the slabs of the layered trigonal structure. This process occurs only at higher temperatures and/or on a longer time scale[3]. A cubic crystal, although with no information on composition, was also found upon crystallization of alloys on the Ge-Sb_2Te_3 pseudobinary line in Ref. 9 including GST523, as already mentioned above.

On these premises, we have first investigated the energetics of the decomposition of GST523 into trigonal compounds on the GeTe-Sb_2Te_3 tie line. Then, we considered the decomposition pathways GST523 $\rightarrow$ $Ge_xSb_2Te_3$ + (5-x)Ge along the Ge-Sb_2Te_3 pseudobinary-line to verify the existence of a more stable composition on this line. Note that in the following we will use the notation GSTXYZ for the alloy with $Ge_xSb_yTe_z$ composition. Finally, we have considered more complex reactions involving also crystalline GeTe such as GST523$\rightarrow$ $Ge_xSb_2Te_{3-y}$ + yGeTe + (5-x-y)Ge. In these latter reactions, crystalline GeSbTe alloys have been modeled by the cubic rocksalt crystal which the amorphous phase is supposed to transform into, as occurs for GeTe-Sb_2Te_3 pseudobinary alloys.

We also considered the reverse reaction of possible regeneration of amorphous GST523 during the reset process of the memory by analyzing the energetics of amorphous models produced by quenching from the melt in DFT molecular dynamics. The different compositions mentioned above have then been investigated in the amorphous phase as well to provide insight onto the evolution of the structural and electronic properties with composition. In this respect, we remark that a very recent paper has reported a DFT study of the structural properties of the amorphous phase of Ge-rich alloys on the Ge-GST124 pseudobinary line[18].

Furthermore, we computed the phonon density of states and the Raman spectra of the crystalline and amorphous phases of the alloys at different compositions to provide some reference data for the detection of the different alloys by micro-Raman spectroscopy.

The paper is organized as follows: After a description of the computational details in Sec. II, the results are presented first for the crystalline phases and then for the amorphous phases in Sec. III.

II. COMPUTATIONAL DETAILS

DFT calculations were performed by using the exchange and correlation functional due to Perdew, Burke, and Ernzerhof (PBE)[19] and the norm conserving pseudopotentials from Goedeker, Teter, and Hutter of Ref. 20. Kohn-Sham (KS) orbitals were expanded in Gaussian-type orbitals of a valence triple-zeta-valence plus polarization basis set, while a basis set of plane waves up to a kinetic energy cutoff of 100 Ry is used to represent the charge density as implemented in the CP2k package[21]. The same framework was employed in our previous works on GST225 and Sb-rich GST alloys[22–24]. There is evidence in the literature that the inclusion of van der Waals (vdW) interactions is important to properly describe the structural properties of GeTe and $Ge_2Sb_2Te_5$[25]. We therefore included the semiempirical correction due to Grimme[26] for van der Waals interactions to model the Ge-rich alloys addressed here.

Crystalline and amorphous phases of ternary GST alloys at all compositions were modeled in cubic 216-atom supercells. Equilibrium geometries and densities at zero temperature of the crystalline phases were obtained by full relaxation of the atomic positions and cell edges. The total energy of the system was calculated for various volumes and then the equation of state was fitted by the Birch-Murnaghan function. For geometry optimization, the Brillouin zone (BZ) integration was restricted to the supercell Γ point. For the calculation of the reaction free energies, total energies have then been computed with a $3\times3\times3$ k point mesh of the supercell BZ for all crystalline and amorphous phases.

All crystalline Ge-rich GeSbTe alloys were modeled with the cubic rocksalt structure analogous to the metastable cubic phase of GST225. The cubic crystalline phases display partial disorder on the cationic or on both the cationic and anionic sublattices. To properly include disorder, the models were generated by using special quasi-random structures (SQS)[27] with the code of Ref. 28.

The energy of the GST124, GST225, and GST326 were computed in the trigonal ground state geometry with the two Sb layers close to the van der Waals gap separating the 7-,9- and 11-layer lamellae in the three compounds with no disorder in the Ge/Sb sublattices[29]. These latter calculations were performed with the code Quantum-Espresso (QE)[30] and the Grimme vdW correction of Ref.[31]. The resulting energies were used to compute the formation energy of the GST124, GST225 and GST326 trigonal crystals with respect to the parent compounds GeTe and Sb_2Te_3. The formation energy is actually negative and amounts to -4.99, -3.78, and -2.98 meV/atom for GST124, GST225 and GST326, respectively. We remark that a positive formation energy was found instead in a previous work[32], possibly due to the neglecting of vdW interactions that are expected to be more important in the layered compounds GST124, GST225, GST326 than in GeTe. The CP2k total energy of GST124, GST225, and GST326 has been then computed from the total energy of GeTe and Sb_2Te_3 supplemented by the formation energy given above.

The amorphous models were generated by quenching from melt by DFT molecular dynamics simulations in the Born-Oppenheimer (BO) approximation with a timestep of 2 fs, as in previous works on GST alloys by us[22–24,33] and other groups[34,35] and on several other phase change alloys[36]. The liquid phase for all compositions has been modeled in a cubic supercell. In the lack of experimental data on the density of these alloys, the cell edges of the cubic supercell have been

chosen such that the density of the liquid phase was 8% less than in the crystalline phase as it is known experimentally for the GST225 compound[37]. The liquid was generated by heating the crystalline models at 2000 K for 2 ps. Then the system has been thermalized at 1000 K for other 8.5 ps. Finally, it has been quenched in almost 100 ps to 300 K in constant pressure, constant temperature (NPT) simulations in order to get the equilibrium density at normal conditions. Only isotropic changes of the cell were allowed in the NPT simulations. The equilibrium volume at 300 K was assigned to the average volume of a NPT simulation 3.5 ps long. A NVT simulation 12 ps long was then performed to compute the average structural properties at 300 K.

Finally, an equation of state at zero temperature was obtained by optimizing the atomic positions for different volumes and by fitting the resulting energy with a Birch-Murnaghan function. The resulting equilibrium geometry was used to compute the equilibrium density and energy at 0 K, the phonon frequencies and the electronic density of states.

Phonon frequencies of crystalline and amorphous models were computed by diagonalizing the dynamical matrix obtained in turn from the variation of atomic forces due to finite atomic displacements 0.0053 Å large. Only phonons with the periodicity of our supercell (Γ point phonons) were considered.

The localization properties of phonons in the amorphous models were analyzed by computing the inverse participation ratio (IPR) which is defined for the j-th vibrational mode as:

$$\mathrm{IPR} = \frac{\sum_\kappa \left| \frac{\mathbf{e}(j,\kappa)}{\sqrt{M_\kappa}} \right|^4}{\left(\sum_\kappa \frac{|\mathbf{e}(j,\kappa)|^2}{M_\kappa} \right)^2} \qquad (1)$$

where $\mathbf{e}(j,\kappa)$ are phonon eigenvectors and the sum over κ runs over the N atoms in the unit cell with masses M_κ. According to this definition, the value of IPR varies from $1/N$ for a completely delocalized phonon, to one for a mode completely localized on a single atom.

Raman spectra in backscattering geometry for non-polarized light were also computed from Γ point phonons within the bond polarizability model (BPM)[38] that we developed in a previous work for GeSbTe alloys[33]. We considered Raman scattering from polycrystalline samples[39]. Different BPM parameters were used for the crystalline and amorphous phases as prescribed in our previous work[33].

Finally, the electronic density of states (DOS) was computed for crystalline models with the QE code with the tetrahedron method on a $12\times12\times12$ k-points mesh. For the amorphous models the DOS were computed still with the QE code from the energies of KS states over a $10\times10\times10$ k-points mesh which were broadened with a Gaussian function with variance of 35 meV.

III. RESULTS

The only thermodynamically stable ternary GeSbTe compounds lay on the GeTe-Sb_2Te_3 pseudobinary tie line. Therefore, we investigated possible decompositions in the most stable compounds along the pseudobinary GeTe-Sb_2Te_3 tie line in the trigonal crystalline phase such as

$$\begin{aligned}
&\text{GST523} \longrightarrow \tfrac{3}{4}\,\text{GST124} + \tfrac{1}{2}\,\text{Sb} + \tfrac{17}{4}\,\text{Ge} \quad (1)\\
&\text{GST523} \longrightarrow \tfrac{3}{5}\,\text{GST225} + \tfrac{4}{5}\,\text{Sb} + \tfrac{19}{5}\,\text{Ge} \quad (2)\\
&\text{GST523} \longrightarrow \tfrac{3}{6}\,\text{GST326} + \text{Sb} + \tfrac{7}{2}\,\text{Ge} \quad (3)\\
&\text{GST523} \longrightarrow 3\,\text{GeTe} + 2\,\text{Ge} + 2\,\text{Sb} \quad (4)
\end{aligned}$$

However, in the set process of the memory the crystallization of the amorphous phase is very fast and it typically leads to the formation of metastable phases as is the case for GST225 which crystallizes in the metastable cubic rocksalt phase. Similarly, either in the forming or set operations we might expect that GST523 could crystallize by phase separation into metastable structures and metastable compositions and not necessarily into the thermodynamically most stable alloys.

Therefore, aside from the decomposition path of GST523 into the thermodynamically stable products, we have to consider alternative paths into metastable phases that might be kinetically more favorable. For instance, we considered first different possible decomposition paths of GST523 into crystalline Ge and less Ge-rich crystalline GST alloys along the Ge-Sb_2Te_3 pseudobinary line as follows:

$$\begin{aligned}
&\text{GST523} \longrightarrow \text{Sb}_2\text{Te}_3 + 5\,\text{Ge} \quad (5)\\
&\text{GST523} \longrightarrow \text{GST123} + 4\,\text{Ge} \quad (6)\\
&\text{GST523} \longrightarrow \text{GST223} + 3\,\text{Ge} \quad (7)\\
&\text{GST523} \longrightarrow \text{GST323} + 2\,\text{Ge} \quad (8)\\
&\text{GST523} \longrightarrow \text{GST423} + \text{Ge} \quad (9)
\end{aligned}$$

Furthermore, we considered the more complex reaction with the formation of crystalline GeTe as

$$\text{GST523} \longrightarrow \text{GST221} + 2\,\text{GeTe} + \text{Ge} \quad (10)$$

The choice of reaction (10) is motivated by the existence of a metastable, tetragonally distorted NaCl-like phase of GeSb[40] which might incorporate Te on the anionic sublattice to give rise to the GST221 alloy. All these decomposition reactions are sketched in the ternary phase diagram in Fig. 1.

Note that the GST323 alloy of reaction (8) is at the intersection between the Ge-Sb_2Te_3 and the Sb-GeTe pseudobinary-lines. Decomposition paths of GST523 into other alloys on the Sb-GeTe pseudobinary line such as GST523 $\longrightarrow$ GST222 + GeTe + 2Ge cannot be excluded. Actually, the resulting GST111 alloy was already studied in our previous DFT work[24]. We might also conceive decomposition on the Sb-GeTe pseudobinary-line with the formation of crystalline Sb or GeSb alloys. As we have to consider metastable products, the list of possible decomposition pathways is actually very long.

In this paper, as a first attempt to investigate theoretically the decomposition process of GST523, we restrict ourselves to reactions (1)-(10) by leaving for future investigation a more extensive exploration of the phase space.

We also investigated whether the reverse of some of the reactions listed above might also take place during reset to recover amorphous GST523 from crystalline Ge and less Ge-rich GST alloys. In order to ensure the feasibility of these

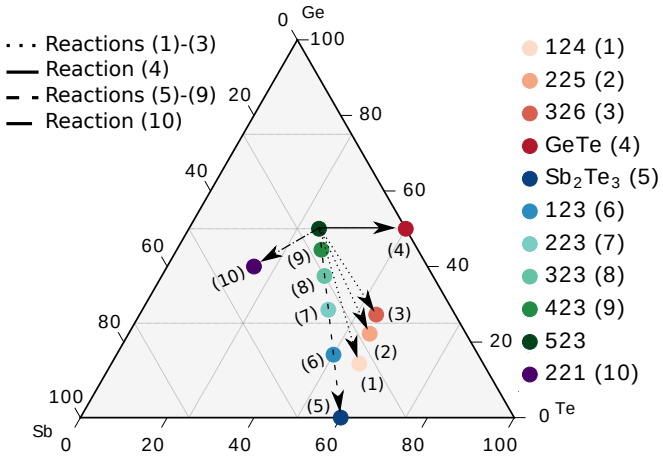

FIG. 1: Sketch of the decomposition pathways of GST523 investigated here on the ternary Ge-Sb-Te phase diagram. The arrows indicate the transformations of GST523 into the main product for the different pathways.

reaction paths, we computed the reactions energies by means of DFT electronic structure calculations. The results for the crystalline and amorphous phases are reported in the separate Secs. IIIA and IIIB.

A. Crystalline phases

All Ge-rich crystalline GeSbTe alloys have been modeled by a 216-atom cubic supercell in a rocksalt geometry analogous to the metastable cubic phase of GST225. In cubic GST225, Sb and Ge atoms occupy randomly the cation sublattice with 20 % of stoichiometric vacancies, while Te atoms fully occupy the anionic sublattice. Stoichiometric vacancies in GST225 ensure on average the presence of exactly three p electrons per site leading to a closed shell system[41].

In the case of GST523, GST423, and GST221 there are less than three p electrons per atom in the formula unit and thus cationic vacancies have not been included while antimony is supposed to behave as an amphoteric element due to the low content of Te. The GST323 alloy has exactly three p-electron per site, while the GST223 and GST123 alloys have more than three p electrons per atom in the formula unit and then we introduced vacancies in the cationic sublattice to enforce the presence of an average of three p electrons per site in the rocksalt crystal.

For all compositions we considered three independent SQS models. The exact composition of the 216-atom models and the distribution of atoms in the two sublattices are described in details in the Supplemental Material (SM)[42]. The equilibrium lattice parameter and the bulk modulus of the different alloys in the cubic rocksalt crystalline phase are reported in Table I. On the Ge-Sb_2Te_3 pseudobinary line, the lattice parameter decreases by increasing the fraction of Ge atoms due to its smaller size with respect to Sb and Te atoms. Note that the atomic fraction of Ge is 50, 44, 37.5, 28.6, 16.6, 40 and 22 % for GST523, GST423, GST323, GST223, GST123, GST221, and GST225. In spite of the different compositions, the lattice parameters in Table I are overall rather similar.

In all these alloys, the ideal rocksalt structure is distorted with the formation of longer and shorter bonds as occurs in GST225[33,43]. The distribution of the three shorter and the longer bonds for each species is reported in Fig. 2. The bimodal distribution of the bonds formed by Ge is enhanced by decreasing the Ge content possibly because of an expansion of the lattice parameter (see Table I). In the case of the bonds formed by Sb and Te, the bimodal distribution for GST523 is less pronounced because both Sb and Te form bonds only with Ge. By decreasing the content of Ge, Sb-Sb and Sb-Te bonds form as well which gives rise to a further enhancement of the bimodal character of the bond distribution because Sb-Sb and Sb-Te bonds are longer than Ge-Te bonds (see, for instance, the partial pair correlation functions of the amorphous phase in Fig. S3 in the SM[42]). In GST123 and GST223 an additional spread in the bond lengths is due to the presence of vacancies in the cationic sublattice. A similar plot for GST225 is shown in Fig. 6 of Ref. 33. The bonding geometry is always octahedral, with no tetrahedra, also for GST221 despite the presence of many Ge-Sb bonds.

TABLE I: Theoretical lattice parameter and bulk modulus of the GST alloys involved in possible decomposition reactions of GST523. The theoretical data for GST225 are taken from Ref. 23 and refer to PBE calculations with no vdW corrections. The average values and the mean deviation refer to calculations over three independent SQS models.

alloy	a (Å)	density (atoms/Å^3)	bulk modulus (GPa)
GST523	5.893±0.004	0.0391±0.001	53±1
GST423	5.999±0.001	0.0371±0.001	33.3±0.8
GST323	6.141±0.001	0.03454±0.0002	49±1
GST223	6.138±0.001	0.0331±0.001	41±1
GST123	6.134±0.004	0.0313±0.0001	34.8±0.9
GST221	5.9670±0.006	0.0376±0.001	49.5±0.5
GST225	6.140	0.0311	-

1. *Energetics of decomposition reactions in the crystalline phases*

The energy per atom of the different alloys and of the reference systems are collected in Table S1 in the SM[42]. Entropic contribution due to disorder in the crystalline phases has also been included in the calculation of the reaction free energy described in the SM[42].

To compute the reaction energy, we have to consider the small deviation from stoichiometry imposed by the use of a 216-atom cell. Therefore reactions (1)-(10) must actually be read with the exact compositions as given by reactions (1′)-(10′) in SM[42].

The reaction energies and free energies computed for reactions (1)-(10) are reported in Table II. The reaction free energy at 300 K due to configurational entropy and to the vi-

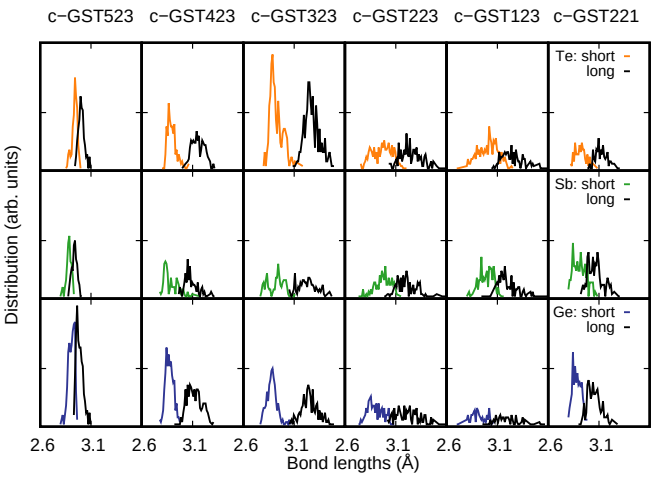

FIG. 2: Distribution of the three shorter and the three longer bonds for the different species in the crystalline cubic phase of Ge-rich GST alloys.

brational free energy are reported separately along with the total reaction free energy at 300 K. The vibrational contribution is computed from phonons at the supercells Γ point as discussed in Sec. II.

Reaction energies are computed as the energy of the product minus the energy of the reactant. A negative sign means that the reaction is exothermic and therefore that the corresponding decomposition path is thermodynamically favored. The reaction free energies are plotted in Fig. 3 as a function of the Ge or GeTe content of the main decomposition product on the two pseudobinary lines.

We remark that the contribution of both the configurational entropy and vibrational free energy in the crystalline phase is rather small (less than 5 meV/atom at 300 K). Therefore, its contribution at somewhat higher temperatures, e.g. 600 K, in the supercooled liquid phase is not expected to change the qualitative picture drawn in Fig. 3.

The reaction free energy for the formation of compounds on the GeTe-Sb_2Te_3 tie line are all very similar, including the two extremes GeTe and Sb_2Te_3. However, we should actually consider the formation of cubic phases and not the ground state trigonal phases because the latter most probably can not form during the set of the memory as they do not in PCMs made of GST225 or GST124. If we consider, for instance, the cubic metastable phase of GST225 its energy is 58.7 meV/atom higher than the trigonal phase. This latter number is obtained from calculation with a 270-atom supercell of the rocksalt phase which can accommodate the exact stoichiometry with 20 % of vacancies on the cationic sublattice. In a previous work[44] this energy difference was larger because of the use of the Γ point only in the integration of the BZ. Moreover, the complete segregation of Sb in the formation of GeTe in reaction (4), besides the segregation of crystalline Ge which is common to all other reactions, might be kinetically more difficult. Therefore, by excluding reaction (4) and by considering only the metastable cubic phases on the GeTe-Sb_2Te_3 tie line, other reactions such as (8) and (10) become competitive.

Along the Ge-Sb_2Te_3 pseudobinary line, the formation of GST323 is the most exothermic reaction because of the higher stability of this alloy which is the only one with an average number of three p electrons per site with no vacancies.

In conclusion, the most thermodynamically favorable reaction are the formation the trigonal phases along the GeTe-Sb_2Te_3 tie line, as expected. However, if we consider the formation of the metastable cubic phases, the other two exothermic reactions (8) and (10) with the formation of GST323 or GST221 become competitive. Moreover, the segregation of both Sb and Ge in reactions (1)-(4) might be also kinetically disfavored. We cannot obviously exclude that GST523 might decompose more favorably in other cubic products, because of our very limited exploration of the ternary phase diagram. However, our results show that Ge and Sb-rich alloys such as GST221 or GST323 might more favorably form in the decomposition of GST523 than cubic alloys on the GeTe-Sb_2Te_3 tie line.

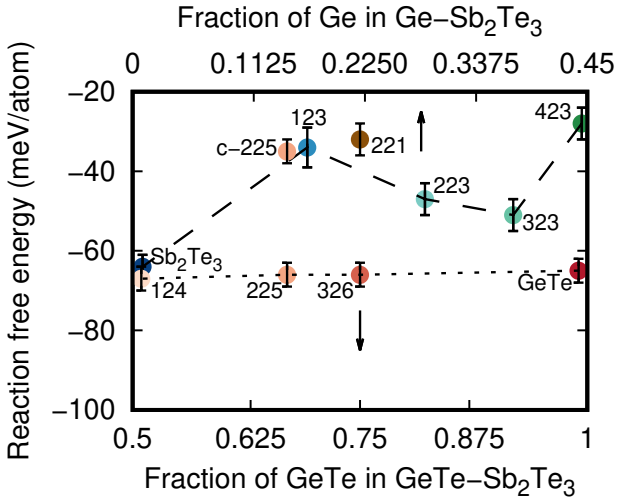

FIG. 3: Reaction free energy from Table II for different decomposition pathways of GST523 labeled by their main product. The free energies are reported as a function of the Ge content in the main product on the Ge-Sb_2Te_3 pseudobinary line (upper abscissa scale) for alloys on the dashed line and as a function of the GeTe content in the main product on the GeTe-Sb_2Te_3 tie line (lower abscissa scale) for trigonal compounds on the short dashed line. The point for GST221 is also shown although it does not belong to the two pseudobinary lines. c-GST225 stands for the metastable cubic phase of GST225. Negative free energy means that the decomposition reaction is exothermic.

2. *Electronic and vibrational properties of selected crystalline alloys*

In this section we discuss the electronic and vibrational properties of a subset of the possible decomposition products of GST523 reported in the previous section. Namely, we con-

TABLE II: Reaction energy, configurational and vibrational contributions to the reaction free energy and total reaction free energy (products minus reactants) of reactions (1)-(10) in meV/atom for all alloys in their crystalline phase. A negative energy indicates an exothermic reaction. The main product of reactions (1)-(5) is in the trigonal phase, while it is in the cubic phase for all the other reactions. The vibrational contribution to the free energy per atom is computed from phonons at the Γ point with frequencies ω_i as $F_{vib} = k_B T/N \sum_i \ln(1 - exp(-\frac{\hbar\omega_i}{k_B T})) + \frac{\hbar\omega_i}{2}$ where N is the number of atoms in the supercell. The configurational free energy is -TS where S is the configurational entropy defined in the SM[42]. For GST523 this number is -8.7 meV/atom at 300 K.

Reaction/main product	Reaction energy 0 K (meV/atom)	Configurational reaction free energy at 300 K (meV/atom)	Vibrational reaction free energy at 300 K (meV/atom)	Total reaction free energy at 300 K (meV/atom)
(1) GST124 trig.	-76	8.7	-	-67
(2) GST225 trig.	-75	8.7	-	-66
(3) GST326 trig.	-74	8.7	-	-66
(4) GeTe trig.	-73	8.7	-	-65
(5) Sb_2Te_3 trig.	-73	8.7	-	-64
(6) GST123	-32	-1.8	-	-34
(7) GST223	-44	-3.8	-	-47
(8) GST323	-51	-2.9	2.5	-51
(9) GST423	-26	-2.8	1.1	-28
(10) GST221	-35	1.1	1.9	-32

sider GST423, GST323, GST221 and GST523 whose electronic density of states are collected in Fig. 4. The electron-poor alloys GST523, GST423, and GST221, i.e. with less than three p electrons per site, are metallic with the Fermi level lying at energies lower than the deep pseudogap. On the contrary, the GST323 alloy with exactly three p electrons per site is semiconducting with an electronic gap of 0.16 eV, which is most probably underestimated by at least a factor of 2 as usual for DFT-PBE calculations. The presence of a closed-shell structure with no stoichiometric vacancies in GST323 justifies its higher stability with respect to the other compositions along the Ge-Sb_2Te_3 pseudobinary line.

The phonon density of states of the four alloys and the IPR is reported in Fig. 5. The phonons at the upper band edge are localized on atoms on the shorter bonds which appear due to disorder (see Fig. 2). The DOS projected on the different types of atoms are shown in Fig. S1 in the SM[42].

The Raman spectra of the four alloys in backscattering geometry for non-polarized light and for a polycrystalline sample are collected in Fig. 6. The large change in the Raman spectrum by moving from GST523 to the other less Ge-rich alloys is due to the presence of Sb-Te bonds at all compositions but GST523. As discussed in our previous work, Sb-Te bonds are more polarizable than the Ge-Te bonds which make their presence particularly evident in the Raman spectrum. Overall the dependence of the spectra on composition seems sufficiently large to allow discriminating the different alloys by Raman spectroscopy.

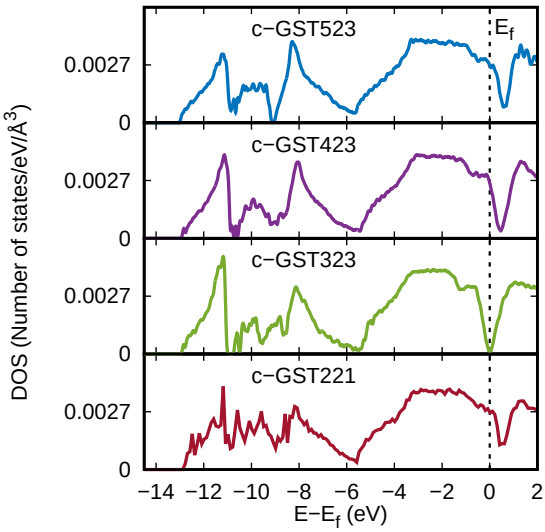

FIG. 4: Electronic density of states of crystalline Ge-rich alloys. The zero energy is the Fermi level.

B. Amorphous phases

In this section we discuss the properties of the amorphous phase of GST523 and the subset of possible decomposition products reported in the previous section. The models of the amorphous phase of GST523, GST423, GST323, and GST221 were generated by quenching from the melt to 300 K at constant pressure and temperature according to the protocol described in Section II.

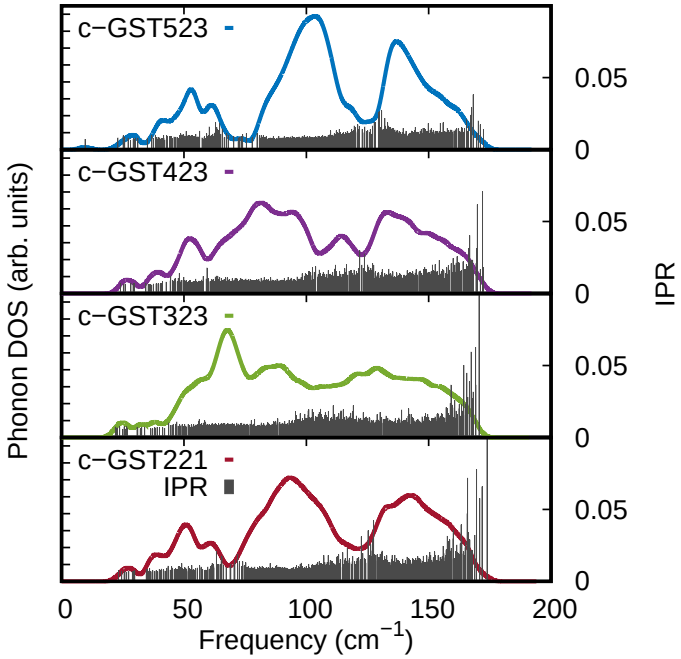

FIG. 5: Total phonon density of states and inverse participation ratio (IPR) of crystalline Ge-rich alloys. The DOS is obtained from phonon frequencies at the supercell Γ point broadened by a Gaussian function with a variance of 1.5 cm^{-1}.

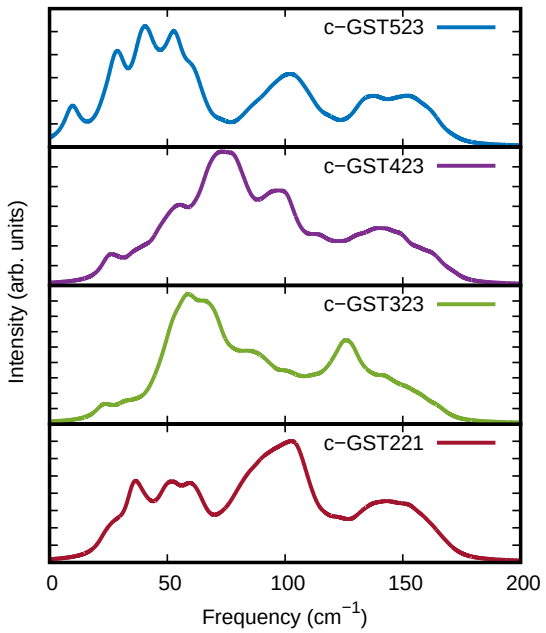

FIG. 6: Raman spectra of crystalline Ge-rich alloys. The contribution from each phonon is broadened with a Lorentzian smearing of 3 cm^{-1}.

1. Structural properties of the amorphous phase

Structural properties at 300 K were obtained from NVT simulations at the end of the NPT quenching run. A snapshot of the model of amorphous GST523 is shown in Fig. S2 in the SM[42]. The equilibrium density at zero temperature is 0.0338, 0.0371, 0.0331, and 0.0323 atom/Å^3 for GST523, GST423, GST323, and GST221 as obtained by a Birch-Murnaghan fitting of the energy vs volume data of the cubic cells.

The total and partial pair correlation functions at 300 K and average coordination numbers of the amorphous model of the different alloys are given in Fig. S3 and Table S2 in the SM[42]. The distribution of coordination numbers at 300 K are reported in Fig. 7, as obtained by integrating the partial pair correlation functions up to the bonding cutoff. For the sake of comparison with a-GST225, we chose the same bonding cutoffs used for a-GST225 in Ref. 22 which are 3.2 Å for all pairs but Sb-Te for which the bonding cutoff was set to 3.4 Å. Ge atoms are mostly 4-coordinated and Te atoms are mostly 3-coordinated as occurs in a-GST225[22]. The percentages of the different types of bonds for each chemical species are given in Table S3 in SM[42]. The fraction of Ge-Ge bonds increases by increasing the percentage of Ge per formula unit while the fraction of Sb-Sb bond increases by increasing the percentage of Sb as one can easily foresee. The distribution of Ge, Sb and Te coordination environments for atoms with different coordination number in a-GST523, a-GST423, GST323 and GST221 and a-GST221 are shown in Tables S4-S7 in the SM[42]. Although there is large fraction of Ge-Ge bonds, there is no clear sign of segregation of Ge as the fraction of Ge atoms surrounded by Ge only is very minor. Information on the bonding geometry is given by the bond angle distribution function reported in Fig. 8 for the amorphous models. The broad peak at 90° and the weaker structure around 170° for Ge and Sb correspond to defective octahedral-like geometries. The peak around 109° for Ge atoms is instead due to tetrahedral geometries.

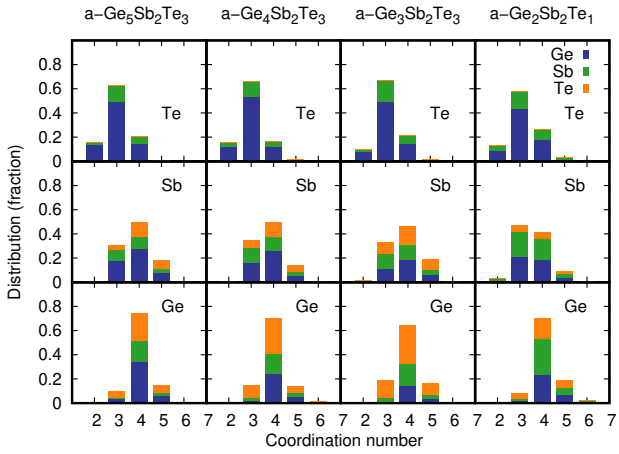

FIG. 7: Distribution of the coordination numbers of Ge-rich amorphous alloys by using the bonding cutoff defined by the partial pair correlation functions in Fig. S3 in the SM[42].

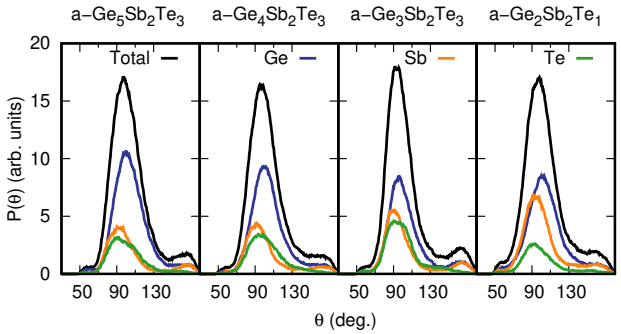

FIG. 8: Bond angle distribution function of Ge-rich amorphous alloys at 300 K. The total distribution and the distributions resolved for the different types of the central atom are shown.

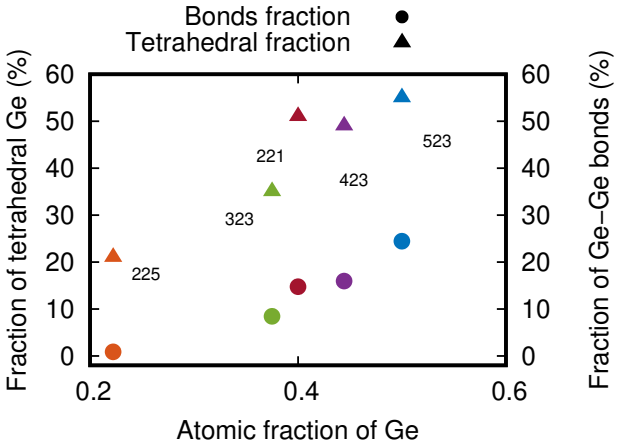

FIG. 9: Fraction (%) of Ge atoms in tetrahedral coordination and fraction (%) of Ge-Ge bonds over the total number of bonds plotted as a function of the atomic fraction of Ge in the different alloys.

A measure of the competition between tetrahedral and defective-octahedral environments is given by the local order parameter q introduced in[45] and defined by

$$q = 1 - \frac{3}{8}\Sigma_{i<k}(\frac{1}{3} + cos(\theta_{ijk}))^2 \qquad (2)$$

where the sum runs over the couples of atoms bonded to a central atom j and forming a bonding angle θ_{ijk}. The order parameter evaluates to q = 1 for the ideal tetrahedral geometry and q = 5/8 for a four-coordinated defective octahedral site. As shown in our previous work[33], the integration of the q distribution of the 4-coordinated Ge atoms from 0.8 to 1.0 gives a measure of the fraction of Ge atoms tetrahedrally coordinated. This choice is in agreement with the analysis of the electronic structure based on Wannier functions for Sb-rich GeSbTe alloys in Ref. 24. The distribution of q parameter for Ge, Sb and Te atoms resolved for different atomic coordination are given in Fig. S4 in the SM[42]. The resulting fraction of tetrahedrally coordinated Ge atoms amounts to 55% in a-GST523, 49% in a-GST423, 35% in a-GST323 and 51% in a-GST221. On the Ge-Sb_2Te_3 pseudobinary line, the fraction of tetrahedral Ge increases by increasing the content of Ge. In GST221 and GST423 the fraction of Ge atoms is similar as well as the fraction of Ge atoms in tetrahedral coordination. The fraction of tetrahedra and the fraction of Ge-Ge bonds are plotted in Fig. 9 as a function of Ge content. A clear correlation is found between tetrahedra and Ge-Ge bonds as it is already known for compounds on the GeTe-Sb_2Te_3 tie line.

Regarding the medium-range order, we report the ring distribution in Fig. 10 computed according to the definition given in Ref. 46. The five-membered ring is the most abundant for all the Ge-rich alloys studied here as opposed to GST225 where four-membered rings dominate the distribution[24]. A similar larger fraction of 5-membered rings was found for the Sb-rich GST111 alloy on the Sb-GeTe pseudobinary line in our previous work[24]. In fact, the low Te content in GST111 favors the formation of Ge-Ge bonds which are responsible for a larger fraction of Ge atoms in tetrahedral sites leading in turn to the formation of five-membered rings. In Ref. 24, it was noted that homopolar bonds, tetrahedra, and five-membered rings in place of four-membered ones are all structures hindering the crystallization, since they are absent in the crystalline phase[35]. The same arguments hold here for Ge-rich GST alloys. The same conclusions on the dependence on the structural properties on the fraction of Ge atoms have been drawn in the very recent DFT study[18] of the amorphous phase of Ge-rich alloys on the Ge-GST124 pseudobinary line including GST212, GST312, GST412, GST512, GST612, and GST712. Interestingly, it was also shown that for an atomic fraction of Ge up to 50 %, corresponding to GST312, the amorphous phase is thermodynamically stable with respect to phase separation into amorphous Ge and amorphous GST124. The decomposition upon crystallization was, however, not addressed in Ref. 18.

Therefore, even in the absence of phase separation into crystalline Ge which surely slows down the crystallization process, Ge-rich GST alloys are expected to feature a lower homogeneous nucleation rate with respect to alloys on the GeTe-Sb_2Te_3 tie line because of larger structural differences between the cubic rocksalt structure and their amorphous phase.

2. *Electronic and vibrational properties of the amorphous phase*

The electronic densities of states of the amorphous phase of the Ge-rich alloys are compared in Fig. 11. There is a finite DOS at the pseudogap in a-GST221 and a-GST523 while a gap clearly opens up in a-GST423 and a-GST323. The states in the gap in a-GST523 are, however, localized as shown by the inverse participation ratio (IPR, see Sec II) in Fig. S5 in the SM[42]. Considering the usual underestimation of the band gap within DFT-PBE we can conclude that the amorphous phase should behave as a semiconductor for all alloys in Fig. 11.

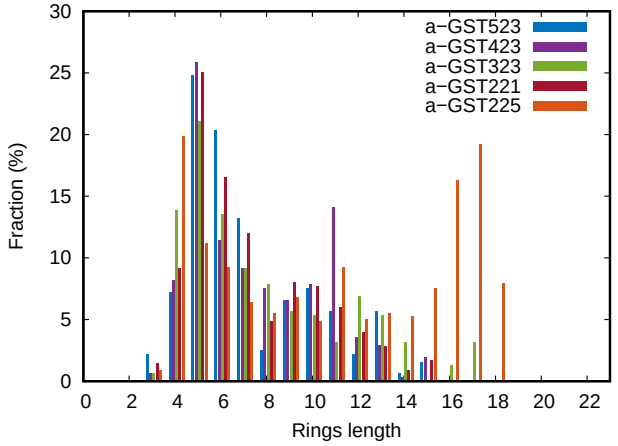

FIG. 10: Ring distribution function of Ge-rich amorphous alloys and of a-GST225 (from Ref. 24) computed as in Ref. 46.

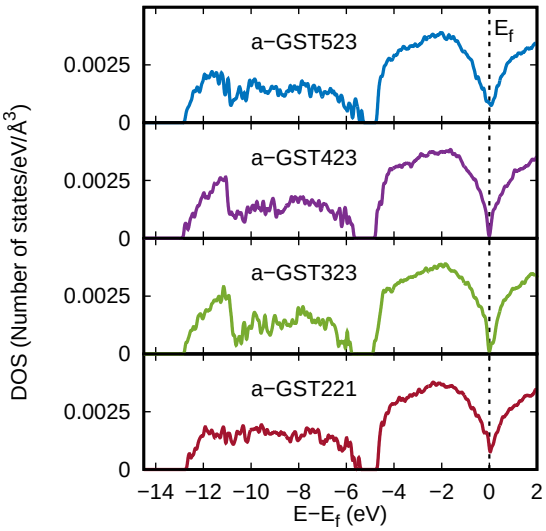

FIG. 11: Electronic density of states of the amorphous Ge-rich alloys computed from KS energies on a 10 $\times 10 \times 10$ k point mesh of the supercell BZ. Each KS energy is broadened with a Gaussian function 50 meV wide. The zero of energy is the highest occupied KS state.

Turning to the vibrational properties, we computed phonon frequencies at the supercell Γ point as described in Sec. II. The phonon DOS superimposed on the IPR is shown in Fig. 12. The projections of the DOS on different types of atoms of the amorphous models are shown in Fig. S6 in the SM[42]. Phonons above 220 cm^{-1} are mostly due to vibrations of Ge atoms in tetrahedral coordination, these modes are also the most localized as shown in Fig. 12.

To aid the identification of the different composition by micro-Raman spectroscopy, we also computed the Raman spectra from DFT phonons and the bond polarizability model as described in Sec. II. The Raman spectra in backscattering geometry for non-polarized light are compared for the four

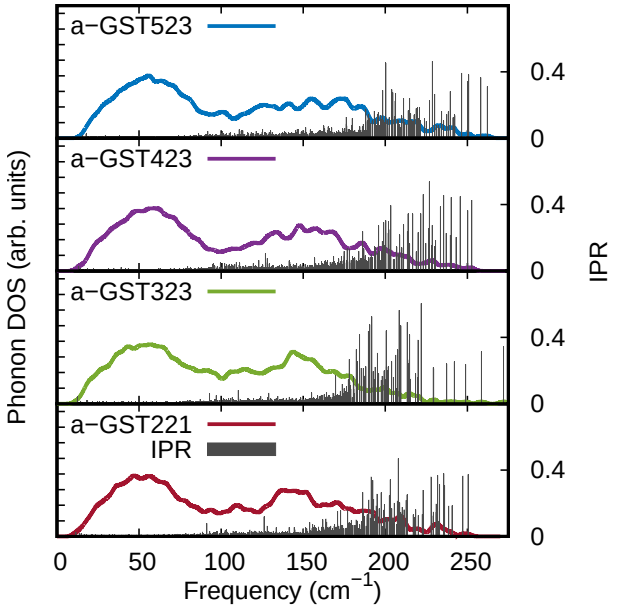

FIG. 12: Inverse participation ratio (gray spikes, see text) superimposed on the phonon DOS of the Ge-rich amorphous alloys.

alloys in Fig. 13. The tail at high frequency of the Raman spectra is due to vibrations of tetrahedral Ge atoms which increase by increasing the fraction of germanium. Overall the Raman spectra of the different compositions look sufficiently different to allow discriminating the different alloys by Raman spectroscopy. Note, however, that the BPM parameters were obtained by fitting ab initio Raman spectra in non-resonant conditions which could bring some disagreement with experimental Raman intensities that are typically measured in resonant conditions for GST alloys. Moreover, we remark that the BPM used here was developed for GST124, GST225, and Sb_2Te_3 which may cause some transferability problems of the BPM parameters for strongly Ge-rich alloys. The same remarks hold for the Raman spectra of crystalline Ge-rich GST alloys discussed in Sec. IIIA.

3. *Energetics of transformation reactions in the amorphous phases*

We also investigated whether the amorphous phase of the pristine composition could be recovered from crystalline Ge and less Ge-rich GST amorphous alloys on the basis of our thermochemical data. This reverse reaction would be of interest for the reset process of the memory. The energy per atom of the optimized amorphous models at zero temperature, reported in Table S1 in the SM[42], allows us to compute the reaction energy for the reverse of transformation (8)-(10) of Sec. IIIA with GeTe and GST alloys in the amorphous phase and Ge in the crystalline phase, such as for instance c-Ge + a-GeTe + a-GST221 $\longrightarrow$ a-GST523. It turns out that all these reverse reactions are endothermic with a reaction energy of 40, 21 and 20 meV/atom for reactions (8)-(10). The vibra-

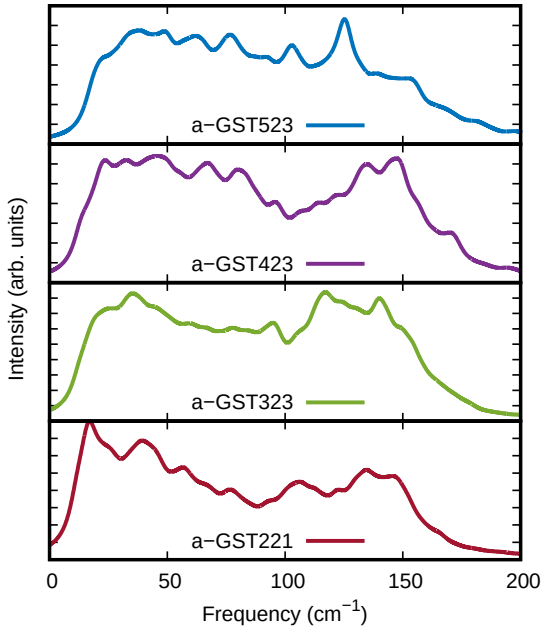

FIG. 13: Raman spectra of Ge-rich amorphous alloys calculated from DFT phonons and the bond polarizability model with Lorentzian smearing of 4 cm $^{-1}$ in backscattering geometry for non polarized light. For the GST523 composition we generated two different amorphous models to check the dependence of the Raman spectrum of the particular realization of the amorphous phase. The phonon DOS and the Raman spectra are very similar for the two models as shown in Figs. S7 and S8 in the SM[42].

tional contribution to the reaction free energy at 300 K is negative, but small amounting to -3.6, -1.9 and -0.4 meV/atom for reactions (8)-(10). This result seems to exclude the reversibility of the process in the amorphous phase. However, if we consider the phase diagram of the binary line Ge-Sb_2Te_3, the formation of the homogeneous liquid with GST523 composition from the separated components can obviously occur above the liquidus temperature at about 750 ^oC[47]. At these conditions, which should be reached in the reset process, crystalline Ge could dissolve into, for instance, the GST221 liquid giving rise to a more Ge-rich liquid that could quench into the metastable amorphous GST523. The liquidus temperature of GST523 could easily be reached during the reset, but the process should last long enough to recover a homogeneous system.

IV. DISCUSSION

As mentioned in the Introduction the motivation to focus on GST523 was twofold: (i) GST523 is the Ge-rich alloy on the Ge-Sb_2Te_3 pseudobinary-line with the lowest Ge content and a T_X suitable for application in embedded memories among those explored in the seminal work of Ref. 9, (ii) GST523 is one of the most abundant products resulting from the crystallization process of highly Ge-rich GST[16] used in several PCM prototypes for embedded applications[15]. GST523 is therefore one of the candidates for the actual alloy undergoing the reversible transformation during set and reset in PCM based on Ge-rich GST. Although some work in the literature is devoted to the study of phase separation of Ge-rich GST alloys during forming, little is known on the possible demixing during set and reset. Our results suggest that decomposition into different products is possible also during set. The calculated reaction free energy of possible decomposition pathways of GST523 into trigonal compounds on the pseudobinary GeTe-Sb_2Te_3 tie line shows that the reaction free energy is very similar for all compounds. However, in the operation conditions of the memory we have to consider also possible metastable products that might appear due to kinetics hindrances. Indeed, in PCMs based on the most studied alloys on the GeTe-Sb_2Te_3 tie line, the amorphous phase crystallizes into a metastable cubic phase and not in the most stable trigonal one. Amorphous Ge-rich GST alloys were also shown in Ref. 9 to crystallize in a cubic phase with unknown composition. If only the metastable cubic phases are considered, other reactions such as GST523 $\longrightarrow$ GST221 + 2 GeTe + Ge and GST523 $\longrightarrow$ GST323 + 2 Ge become competitive. These reactions might also be kinetically favored over the decomposition path GST523 $\longrightarrow$ 3 GeTe + 2 Sb + 2 Ge which involves phase separation into two unary systems. Our analysis shows that different pathways compete for the decomposition of GST523 which points to the possibility that set and reset might actually be a more complex transformation than the simple cycling between the amorphous and crystalline states in a homogeneous phase. In this respect, coarsening of different crystalline grains with different compositions resulting from different decomposition pathways might be a source of the resistance drift of the set state observed experimentally. This process might also be facilitated by the similarity of the lattice parameters of the different alloys that emerged from the DFT calculations reported in Sec. III.

V. CONCLUSIONS

In conclusion, we performed a DFT study of the properties of Ge-rich GST alloys on the Ge-Sb_2Te_3 pseudobinary-line of interest for application in embedded phase change memories operating at high temperatures. We focused in particular on GST523 which is the less Ge-rich composition with sufficiently high T_X studied experimentally for application in embedded memories[9]. Ge-rich GST alloys are known to decompose into crystalline Ge and less Ge-rich alloys during crystallization in thin films, but many details of this process are unknown, especially during the set and reset operations. In this work, we considered a few decomposition pathways of GST523 into other alloys, in particular on the Ge-Sb_2Te_3 and GeTe-Sb_2Te_3 pseudobinary lines.

The theoretical reaction free energies suggest that the thermodynamically favored decomposition path leads to the formation of the trigonal compounds on the GeTe-Sb_2Te_3 tie line. However, if we consider the formation of the metastable

cubic phases and not the trigonal ones, other decomposition reactions such as the formation of GST221 or GST323 become competitive. The formation of GeTe is also thermodynamically favored but it might be kinetically disfavored because it involves the segregation of both Sb and Ge. Although our exploration of the ternary phase diagram is very far from being exhaustive, our results suggest that several decomposition pathways for GST523 compete.

Moreover, we have explored whether the reverse reaction, i.e. regeneration of amorphous GST523 from crystalline Ge and less Ge-rich amorphous alloys, might be possible during reset. To this end, we generated models of the amorphous phases by quenching from the melt within DFT molecular dynamics. Actually, it turns out that the formation of amorphous GST523 is always endothermic at 300 K (but also at 600 K) for all the reactions we have considered which seems to exclude the reversibility of the decomposition reaction, at least at low temperatures. Amorphous GST523 could, however, reform by fast quenching from temperatures above the liquidus temperature if enough time is provided for the heterogeneous system to turn homogeneous in the liquid phase.

Aside from the analysis of the energetics of the transformation reactions, we have provided a comprehensive analysis of the structural, electronic and vibrational properties of the crystalline and amorphous phases of Ge-rich alloys at different compositions. In particular, the calculation of the vibrational spectra suggests that Raman spectroscopy could be used to identify the different alloys that could form in both the amorphous and crystalline phases.

In the presence of phase separation during crystallization, mass transport is expected to slow down the process leading to a higher T_X. However, the analysis of the structural properties of the amorphous phases reveals that the fraction of Ge-Ge bonds, of Ge atoms in tetrahedral coordination and of five- and six-membered rings all increase by increasing the Ge content. Since all these features are not present in the crystalline phases, Ge-rich GST alloys would experience a lower homogeneous crystal nucleation rate and then a higher T_X with respect for instance to GST225 also in the lack of phase separation. Similar conclusions were actually drawn for Sb-rich GST alloys in our previous work[24] and for Ge-rich GST alloys on the Ge-GST124 pseudobinary line in Ref. 18.

VI. ACKNOWLEDGMENTS

This work was partly funded by the European Union's Horizon 2020 research and innovation program under Grant Agreement No. 824957 (BeforeHand: Boosting Performance of Phase Change Devices by Hetero- and Nanostructure Material Design). We thankfully acknowledge the computational resources provided by the ISCRA program at Cineca (Casalecchio di Reno, Italy).

[1] M. Wuttig and N. Yamada, Phase-change materials for rewriteable data storage, Nat. Mater. **6**, 824 (2007).

[2] P. Noé, C. Vallée, F. Hippert, F. Fillot, and J.-Y. Raty, M. Wuttig and N. Yamada, Phase-change materials for non-volatile memory devices: from technological challenges to materials science issues, Semicond. Sci. Technol. **33**, 013002 (2018).

[3] W. Zhang, R. Mazzarello and E. Ma, Phase-change materials in electronics and photonics, MRS Bull. **44**, 9 (2019).

[4] A. Pirovano, A. L. Lacaita, A. Benvenuti, F. Pellizzer, and R. Bez, Electronic switching in phase-change memories, IEEE Trans. Electron. Dev. **51**, 452 (2004).

[5] Choe J 2017 TechInsights Intel 3D XPoint Memory Die Removed from Intel OptaneTM PCM (Phase Change Memory) www.techinsights.com/about-techinsights/overview/blog/intel-3D-xpoint-memory-die-removed-from-intel-optane-pcm (Accessed: 22 November 2020)

[6] S. W. Fong, C. M. Neumann, and H.-S. P. Wong, Phase-Change Memory Towards a Storage-Class Memory, IEEE Trans. Electron. Dev. **64**, 4374 (2017).

[7] P. Cappelletti, R. Annunziata, F. Arnaud, A. Disegni, F. Maurelli, and P. Zuliani, Phase change memory for automotive grade embedded NVM applications, J. Phys. D: Appl. Phys. **53**, 193002 (2020).

[8] P. Noé, C. Sabbione, N. Bernier, N. Castellani, F. Fillot, and F. Hipper, Impact of interfaces on scenario of crystallization of phase change materials, Acta Mater. **110**, 142 (2016).

[9] P. Zuliani, E. Palumbo, M. Borghi, G. Dalla Libera, and R. Annunziata, Engineering of chalcogenide materials for embedded applications of Phase Change Memory, Solid. State. Electron. **111**, 27 (2015).

[10] G. Navarro, M. Coué, A. Kiouseloglou, P. No, F. Fillot, V. Delaye, A. Persico, A. Roule, M. Bernard, C. Sabbione, D. Blachier, V. Sousa, L. Perniola, S. Maitrejean, A. Cabrini, G. Torelli, P. Zuliani, R. Annunziata, E. Palumbo, M. Borghi, G. Reimbold, and B. De Salvo , Trade-off between SET and data retention performance thanks to innovative materials for phase-change Memory. IEDM Tech. Dig., pp.21.5.1-21.5.4 (2013).

[11] H. Y. Cheng, T. H. Hsu, S. Raoux, J.Y. Wu, P. Y. Du, M. Breitwisch, Y. Zhu, E. K. Lai, E. Joseph, S. Mittal, et al., A high performance phase change memory with fast switching speed and high temperature retention by engineering the $Ge_xSb_yTe_z$ phase change material. IEDM Tech. Dig., pp.3.4.1-3.4.4 (2011).

[12] H. Y. Cheng, S. Raoux, and J. L. Jordan-Sweet, Crystallization properties of materials along the pseudo-binary line between GeTe and Sb, J. Appl. Phys. **115**, 093101 (2014).

[13] M. Agati, M. Vallet, S. Joulié, D. Benoit, and A. Claverie, Chemical phase segregation during the crystallization of Ge-rich GeSbTe alloys, J. Mater. Chem. C **7**, 8720 (2019),

[14] E. Palumbo, P. Zuliani, M. Borghi, and R. Annunziata, Forming operation in Ge-rich $Ge_xSb_yTe_z$ phase change memories, Solid-State Elect. **133**, 38 (2017).

[15] V. Sousa, G. Navarro, N. Castellani, M. Coué, O. Cueto, C. Sabbione, P. Noé, L. Perniola, S. Blonkowski P. Zuliani, and R. Annunziata, Operation fundamentals in 12Mb phase change memory based on innovative Ge-rich GST materials featuring high reliability performance, 2015 Symposium on VLSI Technology (VLSI Technology), Kyoto, 2015, pp. T98-T99, doi: 10.1109/VLSIT.2015.7223708.

[16] S. M. S. Privitera, I. López Garca, C. Bongiorno, V. Sousa, M. C. Cyrille, G. Navarro, C. Sabbione, E. Carria, and E. Rimini, Crystallization properties of melt-quenched Ge-rich GeSbTe thin films for phase change memory applications, J. Appl. Phys. **120**, 155105 (2020); S. M. S. Privitera, V. Sousa, C. Bongiorno, G. Navarro, C. Sabbione, E. Carria, and E. Rimini, Atomic diffusion in laser irradiated Ge rich GeSbTe thin films for phase change memory applications, J. Phys. D: Applied Physics **51**, 145103 (2018).

[17] N. Ciocchini, E. Palumbo, M. Borghi, P. Zuliani, R. Annunziata and D. Ielmini, Modeling resistance instabilities of set and reset states in phase change memory with Ge-rich GeSbTe, IEEE Trans. Electr. Device **61**, 2136 (2014).

[18] J. Sun, Y.-X. Zhou, X.-D. Wang, Y.-H. Chen, V. L. Deringer, R. Mazzarello, and W. Zhang, Ab initio molecular dynamics and materials design for embedded phase-change memory, NPJ Comput. Materials **7**, 29 (2021).

[19] J. P. Perdew, K. Burke and M. Ernzerhof, Generalized Gradient Approximation Made Simple, Phys. Rev. Lett. **77**, 3865 (1996).

[20] S. Goedecker, M. Teter, and J. Hutter, Separable dual-space Gaussian pseudopotentials, Phys. Rev. B 54, 1703 (1996); M. Krack, Pseudopotentials for H to Kr optimized for gradient-corrected exchange-correlation functionals, Theor. Chem. Acc. **114**, 145 (2005).

[21] J. Vandevondele, M. Krack, M. Fawzi, M. Parrinello, T. Chassaing, and J. Hutter, Quickstep: Fast and accurate density functional calculations using a mixed Gaussian and plane waves approach. Comput. Phys. Commun. **167**, 103 (2005); www.cp2k.org.

[22] S. Caravati, M. Bernasconi, T. D. Kühne, M. Krack, and M. Parrinello. Coexistence of tetrahedral- and octahedral-like sites in amorphous phase change materials. Applied Physics Letters **91**, 171906 (2007).

[23] S. Caravati, M. Bernasconi, T. D. Kühne, M. Krack, and M. Parrinello, First-principles study of crystalline and amorphous $Ge_2Sb_2Te_5$ and the effects of stoichiometric defects, J. Phys.: Condens. Matter **21**, 255501 (2009); First-principles study of crystalline and amorphous $Ge_2Sb_2Te_5$ and the effects of stoichiometric defects, **21**, 499803(E)(2009); First-principles study of crystalline and amorphous $Ge_2Sb_2Te_5$ and the effects of stoichiometric defects, **22**, 399801(E)(2010).

[24] S. Gabardi, S. Caravati, M. Bernasconi, and M. Parrinello, Density functional simulations of Sb-rich GeSbTe phase change alloys, J. Phys.: Condens. Matter **24**, 385803 (2012).

[25] H. Weber, M. Schumacher, P. Jóvári, Y. Tsuchiya, W. Skrotzki, R. Mazzarello, and I. Kaban, Experimental and ab initio molecular dynamics study of the structure and physical properties of liquid GeTe, Phys. Rev. B **96**, 054204 (2017); M. Schumacher, H. Weber, P. Jóvári, Y. Tsuchiya, T. G. A. Youngs, I. Kaban, and R. Mazzarello, Structural, electronic and kinetic properties of the phase-change material $Ge_2Sb_2Te_5$ in the liquid state, Sci. Rep. **6**, 27434 (2016).

[26] S. Grimme, J. Antony, S. Ehrlich, and H. Krieg. A consistent and accurate ab initio parametrization of density functional dispersion correction (DFT-D) for the 94 elements H-Pu, J. Chem. Phys. **132**, 154104 (2010).

[27] A. Zunger, S.-H. Wei, L.G. Ferreira and J. E. Bernard, Special quasirandom structures, Phys. Rev. Lett. **65**, 353 (1990).

[28] A. van de Walle, P. Tiwary, M. De Jong, D.L. Olmsted, M. Asta, A. Dick, D. Shin, Y. Wang, L.-Q. Chen, and Z.-K. Liu, Efficient stochastic generation of special quasirandom structures, Calphad **42**, 13 (2013).

[29] B. J. Kooi and J. Th. M. De Hosson, Electron diffraction and high-resolution transmission electron microscopy of the high tempera-

ture crystal structures of $Ge_xSb_2Te_{3+x}$ (x=1,2,3) phase change material, J. Appl. Phys. **92**, 3584 (2002).

[30] P. Giannozzi, S. Baroni, N. Bonini, M. Calandra, R. Car, C. Cavazzoni, D. Ceresoli, G. L Chiarotti, M. Cococcioni, I. Dabo, A. Dal Corso et al. , QUANTUM ESPRESSO: a modular and open-source software project for quantum simulations of materials, J. Phys.: Condens. Matter **21**, 395502 (2009); www.quantum-espresso.org.

[31] S. Grimme, Semiempirical GGA-type density functional constructed with a long-range dispersion correction, J. Comput. Chem. **27**, 15 (2006).

[32] J. L. F. Da Silva, A. Walsh, and H. Lee, Insights into the structure of the stable and metastable $(GeTe)_m(Sb_2Te_3)_n$ compounds, Phys. Rev. B **78**, 224111 (2008).

[33] G. Sosso, S. Caravati, R. Mazzarello, M. Bernasconi, Raman spectra of cubic and amorphous $Ge_2Sb_2Te_5$ from first principles, Phys. Rev. B **83** 134201 (2011).

[34] J. Akola and R. O. Jones, Structural phase transitions on the nanoscale: The crucial pattern in the phase-change materials $Ge_2Sb_2Te_5$ and GeTe, Phys. Rev. B **76**, 235201 (2007).

[35] J. Hegedüs and S. R. Elliott, Microscopic origin of the fast crystallization ability of Ge-Sb-Te phase-change memory materials, Nat. Mater. **7**, 399 (2008).

[36] A. Bouzid, S. Gabardi, C. Massobrio, M. Boero, and M. Bernasconi, First-principles study of amorphous $Ga_4Sb_6Te_3$ phase-change alloys, Phys. Rev. B **91**, 184201 (2015); J. Kalikka, J. Akola, and R. O. Jones, Density functional simulations of structure and polymorphism in Ga/Sb films, J. Phys.: Condens. Matter **25**, 115801 (2013); I. Voleská, J. Akola, P. Jovari, J. Gutwirth, T. Wagner, Th. Vasileiadis, S. N. Yannopoulos, and R. O. Jones, Structure, electronic, and vibrational properties of glassy $Ga_{11}Ge_{11}Te_{78}$: Experimentally constrained density functional study, Phys. Rev. B **86**, 094108 (2012).

[37] T. Matsunaga, H. Morita1, R. Kojima, N. Yamada, K. Kifune, Y. Kubota, Y. Tabata, J.-J. Kim, M. Kobata, E. Ikenaga, and K. Kobayashi, Structural characteristics of GeTe-rich GeTe-Sb_2Te_3 pseudobinary metastable crystals, J. Appl. Phys. **103**, 093511 (2008).

[38] S. Go, H. Bilz, and M. Cardona, Bond charge, bond polarizability, and phonon spectra in semiconductors, Phys. Rev. Lett. **34**, 580 (1975); M. V. Wolkenstein, C. R. Acad. Sci. USSR **30**, 791 (1941); M. Eliashevich and M. Wolkenstein, J. Phys. (USSR) **9**, 101 (1944).

[39] G. C. Sosso, S. Caravati, C. Gatti, S. Assoni, and M. Bernasconi, Vibrational properties of hexagonal $Ge_2Sb_2Te_5$ from first principles, J. Phys. Condens. Matter **21**, 245401 (2009).

[40] B. C. Giessen and C. Bottomeé-Gautier, Structure and alloy chemistry of metastable GeSb, J. Solid State. Chem. **44**, 447 (1972).

[41] M. Luo and M. Wuttig, The dependence of crystal structure of Te-based phase-change materials on the number of valence electrons, Adv. Mater. **16**, 439 (2004).

[42] See Supplemental Material at http://link.aps.org/supplemental/10.1103/PhysRevMaterials.xx.xxxxxx for additional information on the structural, vibrational and electronic properties of the crystalline and amorphous phases of the Ge-rich GST alloys discussed in the text and for details on the energetics of the decomposition pathways of GST523.

[43] A. V. Kolobov, P. Fons, A. I. Frenkel, A. L. Ankudinov, J. Tominaga, and T. Uruga, Understanding the phase-change mechanism of rewritable optical media, Nat. Mat. **3**, 703 (2004).

[44] S. Caravati, M. Bernasconi, T. D. Kühne, M. Krack, and M. Parrinello, Unravelling the mechanism of pressure induced amorphization of phase change materials, Phys Rev. Lett. **102**, 205502 (2009).

[45] J. R. Errington and P. G. Debenedetti, Relationship between structural order and the anomalies of liquid water, Nature (London) **409**, 318 (2001).

[46] D. S. Franzblau, Computation of ring statistics for network models of solids, Phys. Rev. B **44**, 4925 (1991).

[47] S. Bordas, M.T. Clavaguera Mora, B. Legendre, and C. Hancheng, Phase diagram of the ternary system Ge-Sb-Te. II. The subternary Ge-GeTe-Sb_2Te_3-Sb, Thermochim. Acta **107**, 239 (1986).